Ultrafast Science
A SCIENCE PARTNER JOURNAL

RESEARCH ARTICLE

Dual-Wavelength Spectrum-Shaped Mid-Infrared Pulses and Steering High-Harmonic Generation in Solids

Linzhen He[1†], Weizhe Wang[1†], Kan Tian[1], Maoxing Xiang[1], Zhongjun Wan[1], Bo Hu[1], Yang Li[1], Han Wu[1], Zi-Yu Chen[2], Fan Yang[3], and Houkun Liang[1*]

[1]College of Electronics and Information Engineering, Sichuan University, Chengdu, Sichuan 610064, China. [2]Key Laboratory of High Energy Density Physics and Technology (MoE), College of Physics, Sichuan University, Chengdu 610064, China. [3]College of Physics, Key Laboratory of High Energy Density Physics and Technology of the Ministry of Education, Sichuan University, Chengdu, Sichuan 610064, China.

*Address correspondence to: hkliang@scu.edu.cn
†These authors contributed equally to this work.

Citation: He L, Wang W, Tian K, Xiang M, Wan Z, Hu B, Li Y, Wu H, Chen ZY, Yang F, Liang H. Dual-Wavelength Spectrum-Shaped Mid-Infrared Pulses and Steering High-Harmonic Generation in Solids. *Ultrafast Sci.* 2023;3:Article 0022. https://doi.org/10.34133/ultrafastscience.0022

Submitted 16 December 2022
Accepted 22 February 2023
Published 30 March 2023

Mid-infrared (MIR) ultra-short pulses with multiple spectral-band coverage and good freedom in spectral and temporal shaping are desired by broad applications such as steering strong-field ionization, investigating bound-electron dynamics, and minimally invasive tissue ablation. However, the existing methods of light transient generation lack freedom in spectral tuning and require sophisticated apparatus for complicated phase and noise control. Here, with both numerical analysis and experimental demonstration, we report the first attempt, to the best our knowledge, at generating MIR pulses with dual-wavelength spectral shaping and exceptional freedom of tunability in both the lasing wavelength and relative spectral amplitudes, based on a relatively simple and compact apparatus compared to traditional pulse synthesizers. The proof-of-concept demonstration in steering the high-harmonic generation in a polycrystalline ZnSe plate is facilitated by dual-wavelength MIR pulses shaped in both spectral and temporal domains, spanning from 5.6 to 11.4 μm, with multi-microjoule pulse energy and hundred- milliwatt average power. Multisets of harmonics corresponding to different fundamental wavelengths are simultaneously generated in the deep ultraviolet region, and both the relative strength of individual harmonics sets and the spectral shapes of harmonics are harnessed with remarkable freedom and flexibility. This work would open new possibilities in exploring femtosecond control of electron dynamics and light–matter interaction in composite molecular systems.

Introduction

Ultrafast lasers whose electric field are shaped by tuning multiple spectral bands are thought as an ingenious instrument to harness the electron dynamics and strong field phenomena. Ultrashort pulses synthesized by multibands of spectral components find special applications in manipulation of electronic nanotunneling [1–4], attosecond metrology of bound-electron dynamics [5,6], enhancement of high-harmonic generation (HHG) [7–9], novel method of terahertz-wave generation [10] and controlling electron localization in molecular dissociation [11]. For the aforementioned applications in strong-field physics, mid-infrared (MIR) laser attracts substantial research efforts, as the pondermotive force scaling quadratically with the driving wavelength. In addition, in the MIR regime, the individual molecule resonates at unique wavelengths, namely, molecular fingerprints. For example, the wavelength of 6.1, 6.4, 8, 8.7, and 9.1 μm has a sharp resonant response with molecules of amide I, amide II, collagen, glycogen and phosphate, respectively [12]. Thus, multiwavelength tunable MIR femtosecond lasers are beneficial for research in light–matter interaction of biomedical materials, such as minimally invasive tissue ablation [13]. Toward the light transient with multiple spectra bands and ultrashort pulse width, a straightforward method is pulse synthesis. Coherent combination of fundamental wavelength and its commensurate or incommensurate second- or third-order harmonics has been firstly attempted [14,15]. Moreover, in the last decade, pulse synthesizers with good performance in phase control and electric field shaping, but moderate freedom in spectral tuning have been intensively studied by employing sophisticated noise and phase control apparatus and complicated optical systems [16–19]. A number of new physics territories such as isolated attosecond pulse generation via amplitude gating [20], field-controlled attosecond phenomena [21], high-harmonic spectroscopy of solids [22], and petahertz electronics [23] have been explored, enabled by the developed pulse synthesizers. In a further step, tremendous research effort has been made toward the simpler and more compact pulse synthesizers in recent years. In 2016, MIR dual-wavelength optical parametric amplifier (OPA) has been realized by introducing a dispersive material with dominant

third-order dispersion, which makes a parabolic temporal distribution of the seed pulse; thus, 2 discrete spectral components can be amplified at the same time [24]. However, tuning and shaping relative spectral amplitudes of dual wavelengths have not been realized. In addition, this method requires a perfect match between the group delay and phase-matching (PM) profiles of wavelength pairs, which usually is not possible to achieve. Therefore, only a thin (1-mm-thick) nonlinear crystal could be used to generate a flat PM condition, which limits the conversion efficiency to <0.1%. Subsequently, in 2017, we constructed MIR light transient with dual-wavelength coverage of 2.5 and 6.0 μm, via synthesizing the passively carrier-envelope phase-stable signal and idler pulses from one OPA [25]. Furthermore, in 2020, dual-wavelength few-cycle pulses based on cascaded amplification in 2 BBO crystals with type-I and type-II PM respectively have been demonstrated [26]. However, despite that apparatuses of developed pulse synthesizers become more compact, the freedom of wavelength tuning and spectral shaping has not been realized, which is highly desired by the applications of steering electron ionization and optimizing tissue microprocessing.

In this work, we report a MIR femtosecond source with dual-wavelength spectral shaping and exceptional freedom of tunability in both the laser wavelength and the relative spectral amplitudes, based on a simple and compact OPA apparatus. The temporal evolution of the dual-wavelength signal pulse is numerically analyzed, and subsequently, Martinez compressors are designed to carefully compensate the spectral chirp and selectively adjust the temporal overlap of spectral components of the broadband seed pulse. Wavelength pairs tunable in the range of 5.6 to 11.4 μm are generated with an average power up to 280 mW and a power efficiency of 2.8% at the repetition rate of 50 kHz. The combination of Martinez compressor and the unique parabolic PM curve not only allows to adjust the spectral position of dual wavelengths but also enables the fine tuning of their relative amplitudes. Different temporal profiles of MIR pulses shaped by tuning dual-wavelength spectra are measured by an interferometric autocorrelator (IAC). Driven by the MIR tunable dual-wavelength pulses, HHG is harnessed in a polycrystalline ZnSe plate: multisets of HHG spectra corresponding to different fundamental wavelengths are generated at the same time; both the relative strength of harmonics sets and the spectral shapes of harmonics are steered by simply controlling the temporal delay of the pump pulse. This work is the first attempt in shaping the HHG spectrum with good tuning freedom, to the best of our knowledge, and it provides a lot more flexibility compared to the methods of spectral interference [27] and chirp control [28]. The generated MIR femtosecond pulses with the feature of dual-wavelength spectral shaping provide a simple and compact platform for applications in strong field and petahertz electronics such as efficiency enhancement of HHG and steering ultrafast electron ionization, as well as the cold ablation of tissues with multiple biotic constituents.

Materials and Methods

Design principle and numerical simulation

As illustrated in Fig. 1A, the type-I PM curve of $LiGaS_2$ (LGS) crystal has a parabolic shape; thus, in principle, 2 spectral bands could be amplified simultaneously at a particular PM angle. As the PM angle tuning is from 49.3° to 51.2°, MIR pulses with dual-wavelength pairs at 5.6, 10.2 μm; 6.0, 9.8 μm; 6.4, 9.2 μm; and 7.0, 8.6 μm are generated, which correspond to the signal pairs of 1145, 1262 nm; 1151, 1243 nm; 1160, 1227 nm; and 1170, 1207 nm, respectively. In a conventional MIR OPA, the signal pulses are routinely generated through self-phase modulation (SPM) in bulk dielectrics, for example, a yttrium aluminum garnet (YAG) crystal. While the signal spectrum is broadened, the spectral components are separated in time domain by the chirp inherited in SPM, which has been experimentally observed in our previous work [29]. Notably, once the 2 wavelength components from a signal pair are separated by a certain delay, the simultaneous amplification of the dual wavelengths in a MIR OPA is prohibited. To understand the dual-wavelength MIR OPA with the signal generated through SPM, the parametric process is subsequently modeled by solving the 3-dimensional coupled wave equations using by the split-step Fourier method and the 4th-order Runge-Kutta algorithm. A 250-fs pulse and the supercontinuum obtained through WLG in a 10-mm YAG crystal are used as the pump and seed pulses, respectively for the MIR OPA simulation. With or without compensating the chirp and dispersion of the seed pulse, the amplification of single wavelength or dual wavelengths at 1224 and 1163 nm corresponding to MIR idler wavelengths of 6.5 and 9 μm, respectively, are simulated with a specific PM angle. As the MIR OPA is directly fed by the signal pulse generated through the white-light generation, the evolution of MIR idler when the pump pulse coincides with each individual signal wavelength in the temporal domain at a specific PM angle is shown in Fig. 1B and C. It is found that only a single wavelength could be amplified in this case, if dual signal components are separated by 200 fs, and the 250-fs pump pulse is overlapped with one of the signal wavelengths in the temporal domain to ensure an efficient conversion. On the other hand, as the spectral chirp from SPM is carefully compensated, the idler pulse with dual wavelengths centered at 6.5 and 9 μm is generated as simulated in Fig. 1D. The simulation thus indicates that it is crucial to have a method that could compensate for the chirp inherited from SPM and control the temporal separation of the signal spectral components, for the dual-wavelength amplification and spectral tuning. Therefore, more simulations of the dual-wavelength MIR OPA are conducted to reveal and discuss the process of spectral tuning in 2 different ways. Figure 1E shows the simulated idler spectra of the dual-wavelength OPA when the chirp among different spectral components is compensated. Dual wavelengths in the range of 5.6 to 10.2 μm are simulated by adjusting the PM angle. On the other hand, when there is residual spectral chirp, the intensity ratio of the generated dual wavelengths can be adjusted with a full freedom by tuning the pump delay. As an example, dual-wavelength spectra centered at 6.5 and 9 μm with various relative strengths are simulated as shown in Fig. 1F.

In addition, to quantify the temporal separations of the near-infrared signal pairs, induced by the chirp from SPM, numerical simulations of the SPM process in a 10-mm YAG crystal pumped by a 250-fs, 1030-nm pulse, and the propagation in the dispersive LGS crystal (264 fs^2/mm at 1200 nm) with a length of 8 mm are carefully conducted, as shown in Fig. 2. In the calculation of SPM process, we utilize the time transformation approach [30], and the estimated intensity on the front surface of YAG crystal is 2.5 TW/cm^2. The phase modulation induced by the Kerr nonlinear process results in the broadening of the spectrum shown in Fig. 2A. The time-frequency analysis is then implemented for the modulated pulse, from which the time evolution of wave amplitude for a given wavelength can be

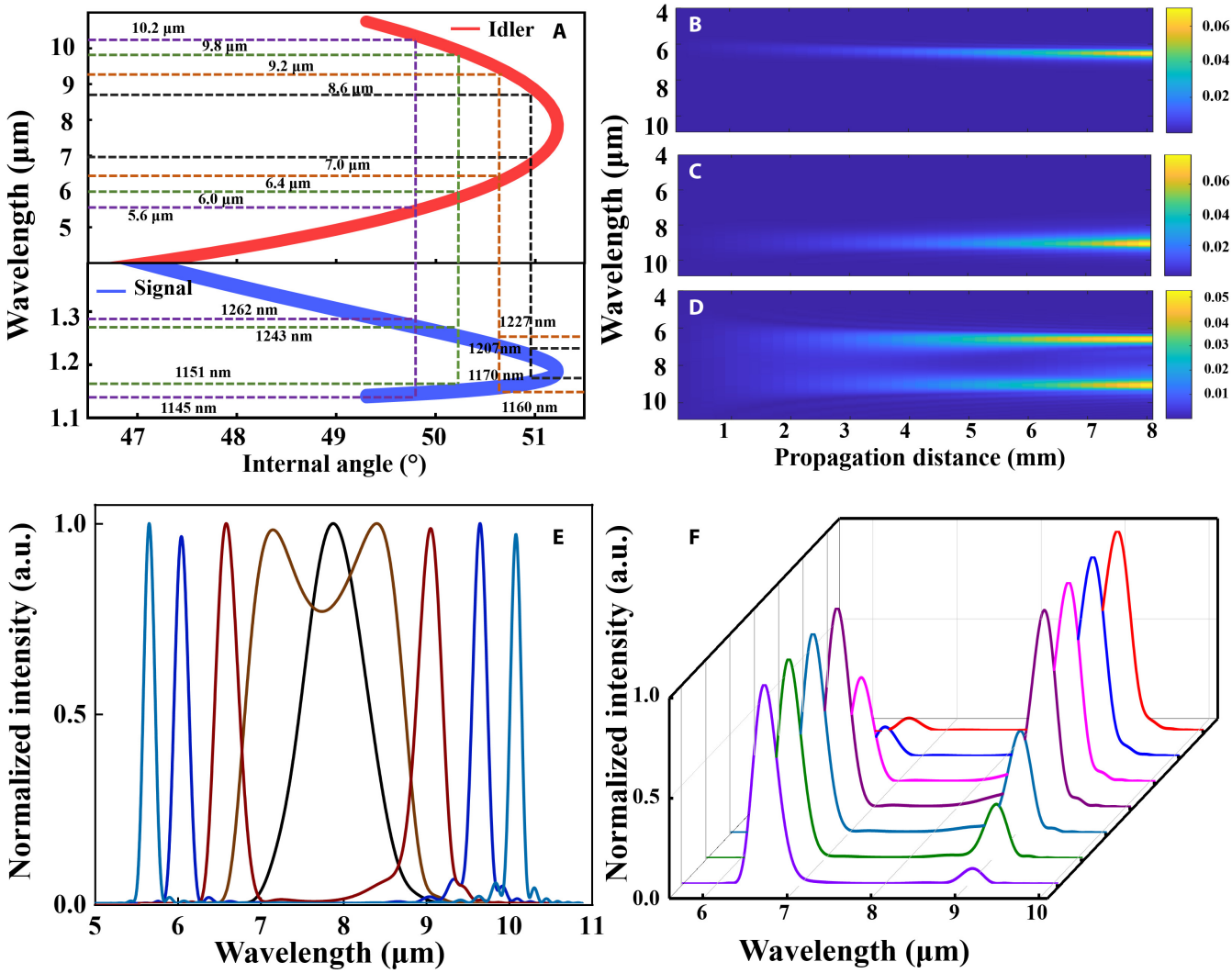

Fig. 1. The design and simulation of the dual-wavelength MIR OPA. (A) The parabolic type-I PM curve of LGS crystal pumped at 1030 nm. Different MIR wavelength pairs in the idler pulse and corresponding near-infrared signal spectral components are marked by color dotted lines at different PM angles. (B to D) The comparison of MIR parametric amplification by directly feeding the signal pulse after the white-light generation process (B and C) and carefully compensating the inherited spectral chirp (D). The pump delay is tuned to overlap with the signal spectral component of 1224 nm (B) and 1163 nm (C). (E) Simulated spectra of amplified dual-wavelength tunable idler pulses through adjusting the PM angles of LGS crystal, when the spectral chirp is compensated and the signal components at 1224 and 1163 nm are overlapped in time domain. Different dual-wavelength pairs at 5.6, 10 μm; 6.0, 9.6 μm; 6.6, 9.0 μm; 7.1, 8.4 μm; and 8.2 μm are obtained through simulation. (F) Simulated spectra of amplified dual-wavelength tunable idler pulses by tuning the temporal overlap between different spectral components of the signal and pump pulses, when there is certain residual chirp and group delay, at a specific PM angle. The amplitudes ratio between 2 spectral components of the obtained dual-wavelength idler can be tunable arbitrarily.

extracted. From Fig. 2B to F, the temporal separations of signal pairs of 1132, 1262 nm; 1139, 1243 nm; 1144, 1227 nm; 1155, 1204 nm; and 1161, 1196 nm are found to be 378 fs, 276 fs, 233 fs, 153 fs and 106 fs, respectively. It is worth mentioning that in our experiment, we found that a temporal separation of 106 fs is large enough to hinder the dual-wavelength amplification for a 250-fs pump pulse.

Experimental setup and optical apparatus

To achieve the dual-wavelength amplification and spectral shaping, a Martinez-type compressor [31] is designed for each OPA stage to compensate and adjust the spectral chirp generated in both the SPM process and the propagation in the OPA crystal and other dielectric media. Figure 3A illustrates the schematic of the dual-wavelength spectrum-shaped OPA system. It starts with a 1030-nm Yb:KGW laser (Pharos) with 400-μJ pulse energy and 250-fs pulse width at 50-kHz repetition rate, serving as the pump source. A 10-μJ pulse energy is split and focused to a 10-mm YAG crystal to generate a stable supercontinuum via single filamentation. After passing through a 1100-nm long-pass filter, signal pulses with 20-nJ pulse energy, extending up to 1800-nm wavelength are obtained as the broadband seed of MIR OPA. The Martinez compressor is subsequently employed to compress the near-infrared signal pulse and control the temporal overlap of multiple spectral components. The compressor consists of 2 reflective gratings (Edmund #37-130) with 300 lines/mm and a confocal system (f = 100 mm) between them. A double-pass configuration is used by placing a retro-reflecting mirror after the second grating to eliminate the spatial chirp. The transmission efficiency of the Martinez compressor is measured to be 70%. The compressed signal pulse is then amplified in the first OPA stage with an 8-mm-thick LGS crystal. Owing to the dispersion control through the designed

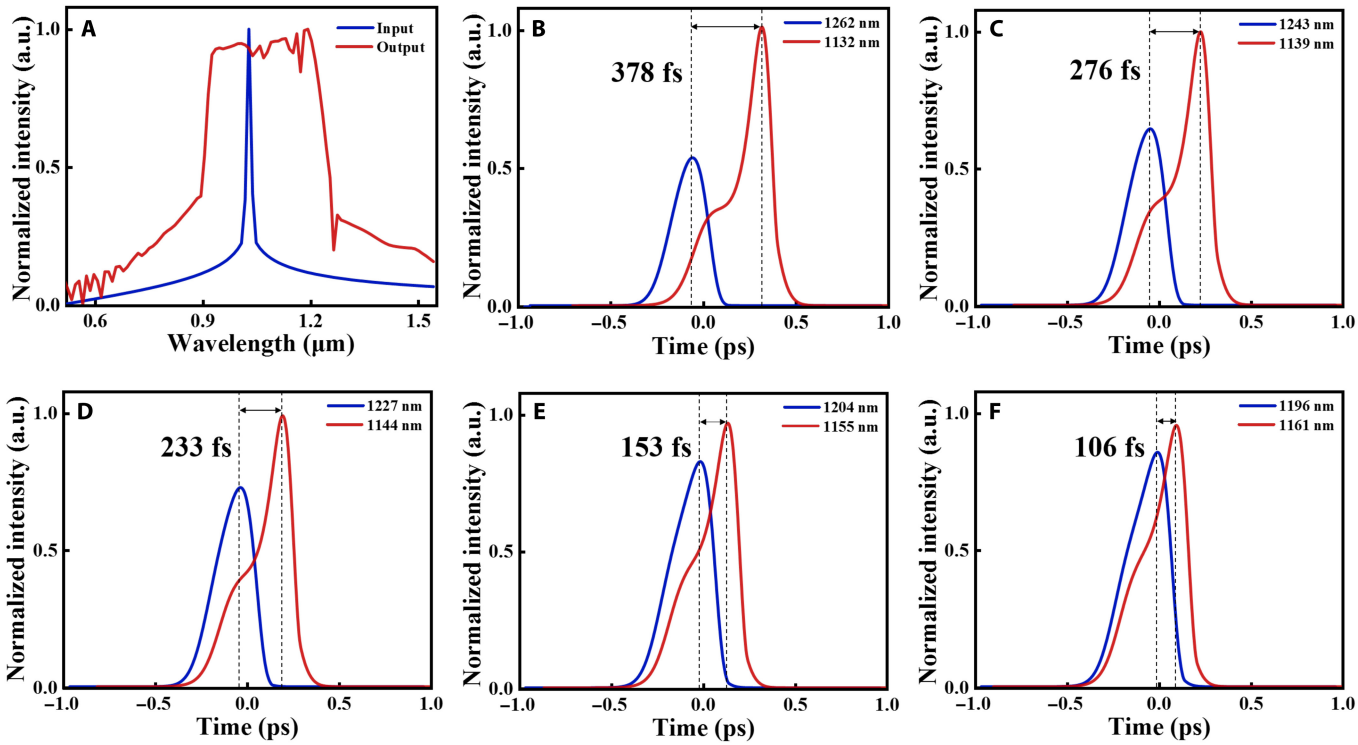

Fig. 2. Numerical simulations of the near-infrared signal pairs induced by the chirp from SPM process and propagation in the dispersive LGS crystal with a length of 8 mm. A time-transformation approach is used for the time-frequency analysis. (A) Spectra of input (blue) and output (red) signal waves. The phase modulation induced by the Kerr nonlinear process results in the broadening of the spectrum. (B to F) Time evolutions of 5 pairs of signal waves: (B) 1132, 1262 nm; (C) 1139,1243 nm; (D) 1144, 1227 nm; (E) 1155, 1204 nm; and (F) 1161, 1196 nm. Temporal separations of the 5 pairs of signal waves are calculated as 378, 276, 233, 153, and 106 fs, respectively. a.u., arbitrary units.

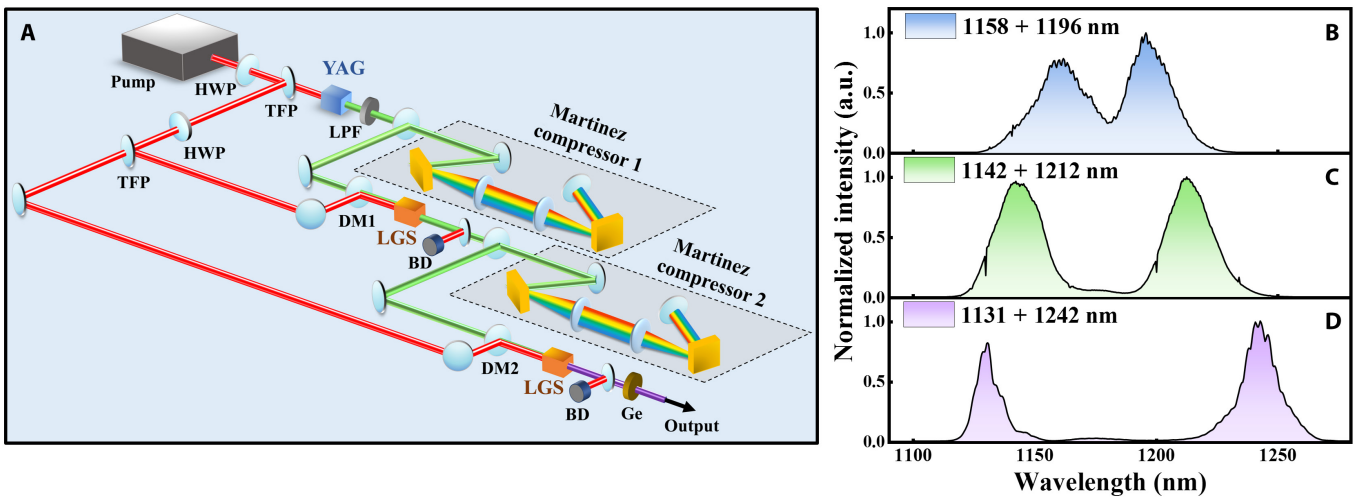

Fig. 3. The experimental implementation of the dual-wavelength tunable MIR pulse generation. (A) Schematic of the dual-wavelength tunable MIR OPA system. It is pumped by a 1030- nm Yb:KGW laser with 400-μJ pulse energy and 250-fs pulse width at 50-kHz repetition rate. A 10-μJ pulse energy is split and focused to a 10-mm YAG crystal to generate the signal pulse via a stable supercontinuum through single filamentation. Two Martinez compressors are employed to compensate the spectral chirp in the processes of white-light generation and parametric amplification. Two stage OPAs with 8-mm-long LGS crystals generate and amplify the spectrum-shaped dual-wavelength MIR pulses. HWP, half-wave plate; TFP, thin-film polarizer; YAG, yttrium aluminum garnet; LPF, long-pass filter (1100 nm); DM1, dichroic mirror (HT@1135–1600 nm, HR@1030 nm); LGS, $LiGaS_2$ crystal; DM2, dichroic mirror (HT@5–11 μm, HR@1030 nm); Ge, germanium window (3 to 12 μm, antireflection coated); BD, beam dump. (B to D) The measured spectra of the amplified dual-wavelength tunable signal pulse from the first OPA stage. The dual-wavelength pairs of (B) 1158 nm, 1196 nm; (C) 1142 nm, 1212 nm; and (D) 1131 nm, 1242 nm are presented.

Martinez compressor, 2 near-infrared spectral components of the signal pulse are amplified simultaneously. The wavelengths of the signal pairs are selected by twisting the PM angles of LGS crystal as shown in Fig. 3B to D. Subsequently, another Martinez compressor is employed to compensate the normal dispersion and group delay introduced by the LGS crystal. The dual-wavelength MIR idler pulse is then generated in the second OPA stage with another 8-mm-thick LGS crystal. A

dichroic mirror is used to separate the MIR idler pulse from the near-infrared signal and pump pulses. The MIR spectrum is then measured by using a scanning-grating monochromator with a liquid-nitrogen-cooled MCT detector. A 19-mm-thick germanium crystal which provides about 9200-fs^2 group delay at a central wavelength of 8 μm is employed to compensate the anomalous dispersion induced in the LGS crystal and compress the MIR idler pulse.

Results and Discussion

Generation and characterization of dual-wavelength spectrum-shaped MIR pulses

The amplified idler spectra with tunable dual wavelengths are presented in Fig. 4. As the signal spectral components spanning from 1100 to 1300 nm are well compressed and controlled, simultaneous amplification of idler dual wavelengths is realized. By adjusting the PM angle of the LGS crystal, typical dual-wavelength spectra at 5.6, 11.4 μm; 6.0, 10.7 μm; 6.4, 10.3 μm; 7.1, 9.5 μm; 7.4, 9.1 μm; and 8.2 μm are measured, as shown in Fig. 4A. The wavelength tuning range is limited by the phase mismatch of the LGS crystal, which lowers the parametric efficiency. On the other hand, when the spectral chirp and group delay are partially compensated by controlling the distance of the second grating in the Martinez compressor, the amplitude ratio between the 2 spectral bands in the amplified dual-wavelength MIR spectrum can be arbitrarily adjusted by varying the time delay between the pump and seed pulses. As measured in Fig. 4B, the full tunability of both the spectral position and the relative intensity of dual wavelengths is demonstrated by tuning the Martinez compressor and the time delay of the pump pulse.

The amplification and output power are characterized as another important specification of the dual-wavelength tunable MIR light source. The average power of the generated MIR pulses with multiple pairs of dual wavelengths are plotted in Fig. 5 as a function of pump power at the second LGS crystal. Higher MIR output power is obtained at dual wavelengths of 7.4 and 9.1 μm and a single central wavelength of 8.2 μm when the PM is close to the optimal condition. MIR power (280 mW) is obtained at 10-W pump power for a dual-wavelength pulse at 7.4 and 9.1 μm with 2.8% power efficiency and ~23% quantum efficiency. The saturation of amplification is not observed, and the output power can be further scaled up with a larger pump power. It is worth mentioning that the dual-wavelength output at 7.4 and 9.1 μm is higher than that of single central wavelength of 8.2 μm where the optimal PM condition is achieved. This is attributed to a broader amplification bandwidth for the case of dual-wavelength amplification, when the dispersion in the signal pulse is fully compensated. As the PM condition moves to the sides of the parabolic PM curve, the output power of the generated dual-wavelength MIR pulse decreases. The inset shows a good Gaussian profile of the dual-wavelength MIR pulse measured by a micro bolometer camera (WinCam D-IR-BB).

The temporal profiles of spectrum-shaped dual-wavelength MIR pulses are measured and retrieved using a home-built IAC. Interferometric idler pulses excite the second harmonic (SH) signals in a 1-mm-thick GaSe crystal, which is chosen for its broadband PM bandwidth in the long-wavelength MIR region. Interferometric SH signal is sent through a BaF_2 polarizer and a 10-mm-thick sapphire, which removes the long-wavelength MIR fundamental pulses via polarization extinction and absorption. An InAsSb amplified photodiode (Thorlabs PDA07P2), which is sensitive in the wavelength range of 2.7 to 5.3 μm, is used to detect the SH signal and further extinguish the fundamental intensity.

The temporal measurements of 3 representative dual-wavelength MIR pulses are presented in Fig. 6. Figure 6A to C is the measured spectra with the spectral bands centered at 8.2 μm; 7.4, 9.1 μm; and 7.1, 9.5 μm, respectively. The measured IAC traces (black solids) are shown in Fig. 6D to F with a ratio of 1:8 between the background and the peak of the IAC signal, which proves the good alignment of the IAC apparatus and the reliability of the measurement results. The electric field is reconstructed through a genetic algorithm based on "evolutionary

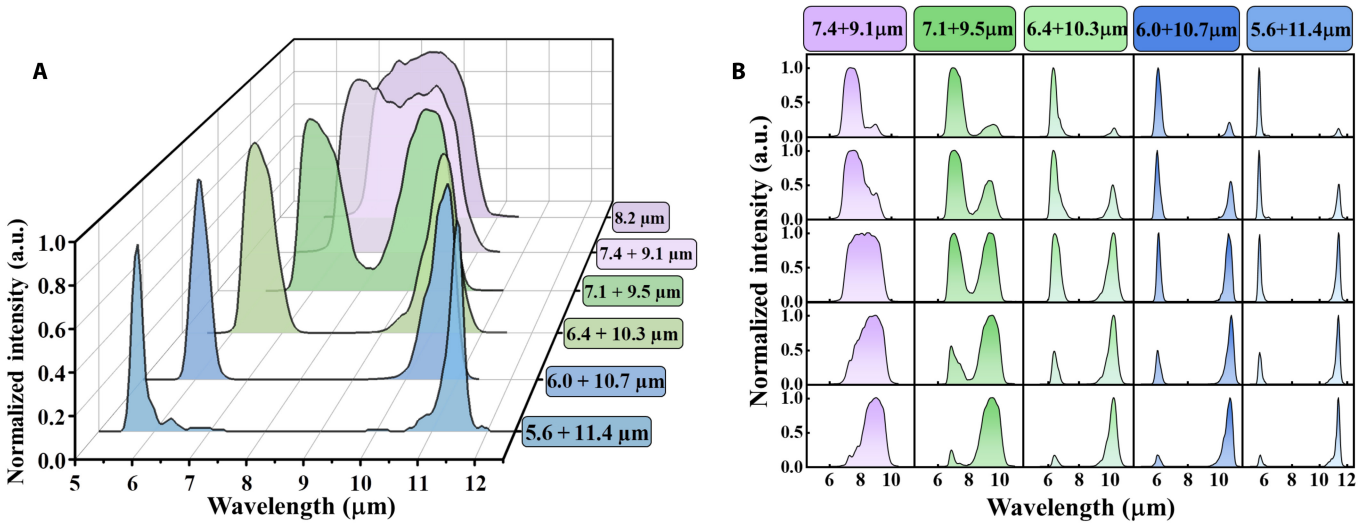

Fig. 4. Spectral shaping of dual-wavelength MIR pulses. (A) Measured spectra of amplified dual-wavelength tunable idler pulses through adjusting the PM angles of LGS crystal, when the group delay between 2 spectral components is fully compensated. Different dual-wavelength pairs at 5.6, 11.4 μm; 6.0, 10.7 μm; 6.4, 10.3 μm; 7.1, 9.5 μm; 7.4, 9.1 μm; and 8.2 μm are obtained. (B) Measured spectra of amplified dual-wavelength tunable idler pulses by tuning the temporal overlap between different spectral components of the signal and pump pulses, when there is certain residual chirp and group delay, at a specific PM angle. MIR dual wavelengths with arbitrary relative amplitudes are generated. The labels besides (A) and on top of (B) indicate the central wavelengths of the spectral bands in the dual-wavelength MIR spectra.

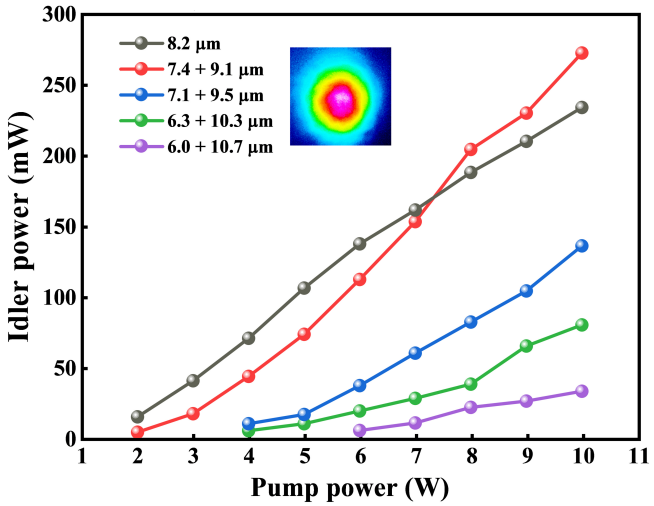

Fig. 5. The output power of the dual-wavelength MIR pulses with the wavelength pairs at 6.0, 10.7 μm; 6.3, 10.3 μm; 7.1, 9.5 μm; 7.4, 9.1 μm; and 8.2 μm as a function of pump power at the second LGS crystal. The inset shows the output MIR beam with a good Gaussian profile.

phase retrieval from interferometric autocorrelation (EPRIAC)" algorithm [32,33]. In the Taylor expansion of the reconstructed spectral phase, dispersion terms up to seventh order are considered. The calculated IAC signal (color dotted) has a good match with the measured ones, which indicates that the dual spectral components are well synthesized. The retrieved temporal profiles of the spectrum-shaped dual-wavelength MIR pulses are shown in Fig. 6G to I. The retrieved pulse widths vary in a range of 128 to 257 fs, corresponding to 5 to 10 optical cycles, assuming a central wavelength at 8.2 μm. It is observed that the larger spectral separation of the dual-wavelength bands is, the longer pulse width is measured. This is because the difference of group delay caused by the propagation in the 8-mm-long LGS crystal is ~190 fs between wavelengths of 7.1 and 9.5 μm, which is also responsible for the pulse splitting observed in Fig. 6I.

Steering HHG in solids

To test the usefulness of the demonstrated high-power MIR light source with dual-wavelength spectra shaping features, we systematically perform HHG in a 3-mm-thick polycrystalline ZnSe plate, pumped by a series of MIR dual-wavelength pulses

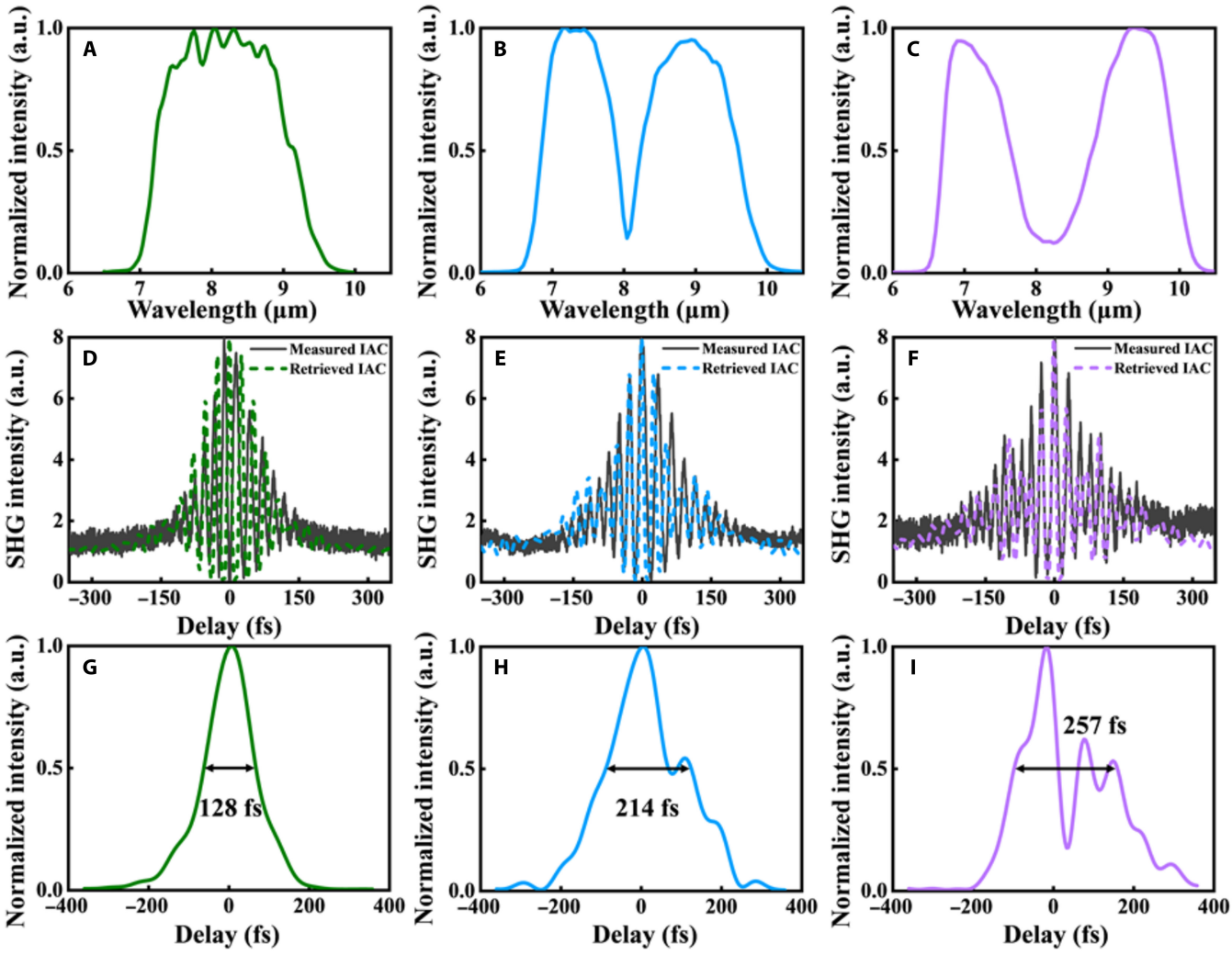

Fig. 6. Temporal characterization of the dual-wavelength tunable MIR pulses at 8.2 μm; 7.4, 9.1 μm; and 7.1, 9.5 μm with the spectral chirp compensated by the Martinez compressors. Row 1 (A to C): Measured MIR spectra at different PM conditions. Row 2 (D to F): Corresponding measured (black solid) and retrieved (color dotted) IAC traces. Row 3 (G to I): Corresponding retrieved temporal profiles. SHG, second harmonic generation.

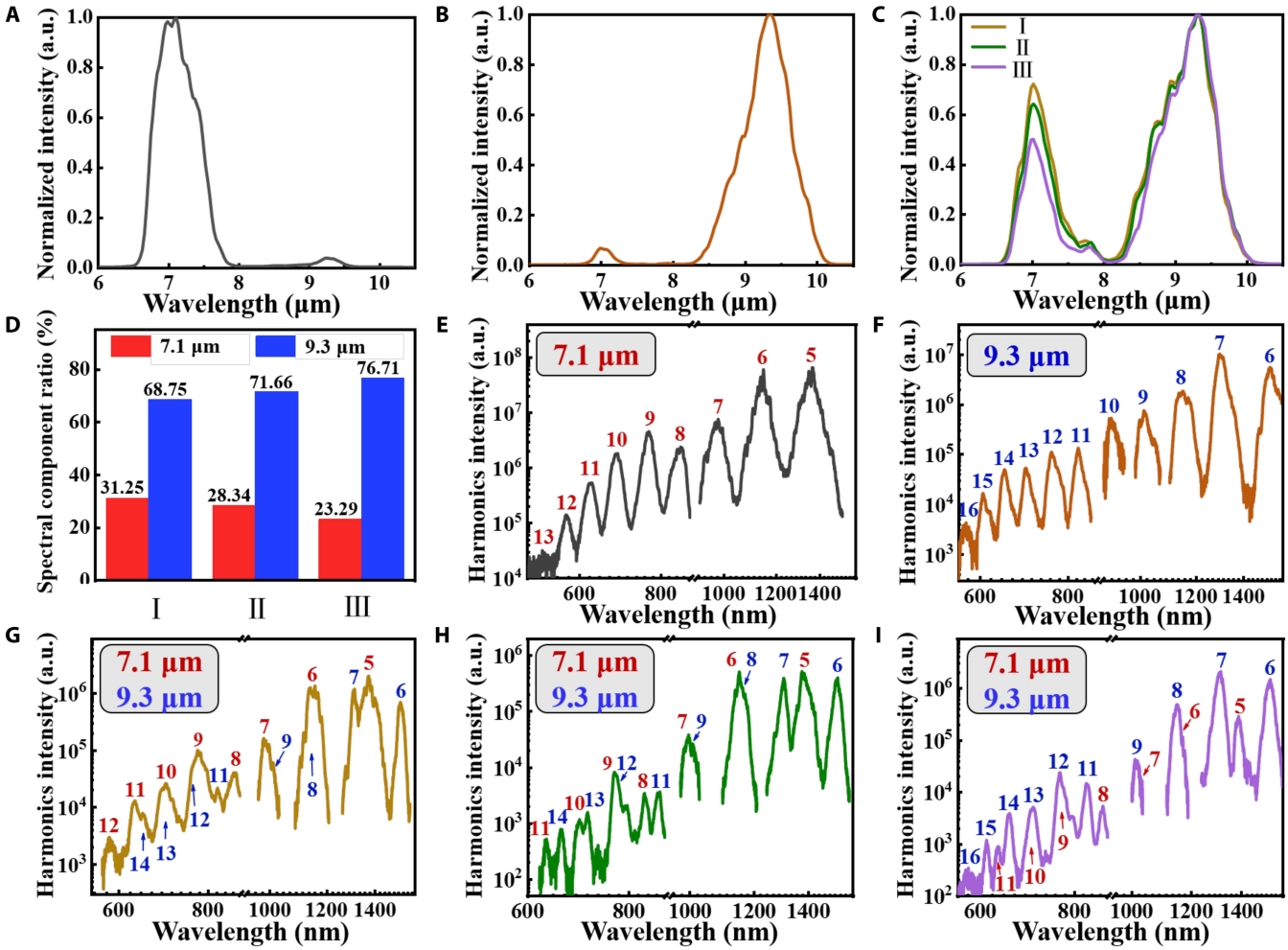

Fig. 7. The fundamental and corresponding HHG spectra driven by dual-wavelength MIR tunable pulses when there is certain residual chirp, and the dual-wavelength spectral components are temporally misaligned. The dual-wavelength MIR spectra could be fine-tuned by adjusting the delay of the pump pulse. In (A) and (B), the spectrum is dominated by the spectral component of 7.1 and 9.3 μm, respectively. (E) and (F) plot the corresponding harmonics with the order up to 13 and 16 of the fundamental wavelengths of 7.1 and 9.3 μm, respectively. By fine-tuning the delay of the pump pulse, dual-wavelength spectra with similar shapes are obtained in (C). The fine distinction among the dual-wavelength spectra is characterized and presented in (D). (G to I) Corresponding HHG spectra driven by dual-wavelength MIR pulses in (C). Two sets of harmonics of 7.1 and 9.3 μm are both exhibited. It is found that the harmonics sets of 7.1 or 9.3 μm dominates in (G) and (I), respectively, while the harmonics of 7.1 and 9.3 μm are comparable in (H). The labels in red and blue indicate the harmonic orders of 7.1 and 9.3 μm, respectively.

with various spectral and temporal profiles. When there is a certain residual spectral chirp, the dual-wavelength components are temporally misaligned. Thus, as shown in Fig. 7, the dual-wavelength MIR spectra could be fine-tuned by adjusting the delay of the pump pulse. In Fig. 7A and B, spectral peaks at 7.1 and 9.3 μm dominate, respectively, while for Fig. 7C, dual-wavelength spectra with similar shapes are exhibited. The fine distinction of the dual-wavelength spectra in Fig. 7C is characterized and presented in Fig. 7D, with the intensity ratio between spectral peaks of 7.1 and 9.3 μm measured as 31:69, 28:72, and 23:77, respectively. In the HHG experiments, MIR pulses with different spectra but similar average power of ~100 mW are focused to the ZnSe plate by using a lens with 50-mm focal length, generating an estimated intensity of 100 to 150 GW/cm^2. The HHG signals are subsequently collected by 2 different spectrometers (Ocean Optics USB 2000+ and Yokogawa AQ6370D). The respective stitched transmitted HHG spectra are plotted in Fig. 7E to I. Driven by single central wavelength at 7.1 or 9.3 μm, the individual harmonics with the order up to 13 and 16 are clearly measured as plotted in Fig. 7E and F, respectively. On the other hand, pumped by the dual-wavelength MIR pulses, harmonics of 7.1 and 9.3 μm are exhibited simultaneously as shown in Fig. 7G to I. Intriguingly, it is found that when the amplitude ratios of the dual wavelengths are 31:69 and 23:77, harmonics of 7.1 or 9.3 μm dominate, respectively, as plotted in Fig. 7G and I. Moreover, the harmonics of 7.1 and 9.3 μm become comparable at a fundamental amplitude ratio of 28:72, as presented in Fig. 7H. In other words, 2 sets of HHG spectra corresponding to different fundamental wavelengths can be generated at the same time, and their relative strengths can be tuned. In addition, effective shaping of HHG spectra is found to be very sensitive to the fundamental spectral components and could be realized by simply adjusting the pump delay position.

To further explore the feasibility of steering HHG through spectral shaping based on the developed dual-wavelength MIR source, the residual spectral chirp is fully compensated, and broadband MIR pulses are adopted as the driving source of

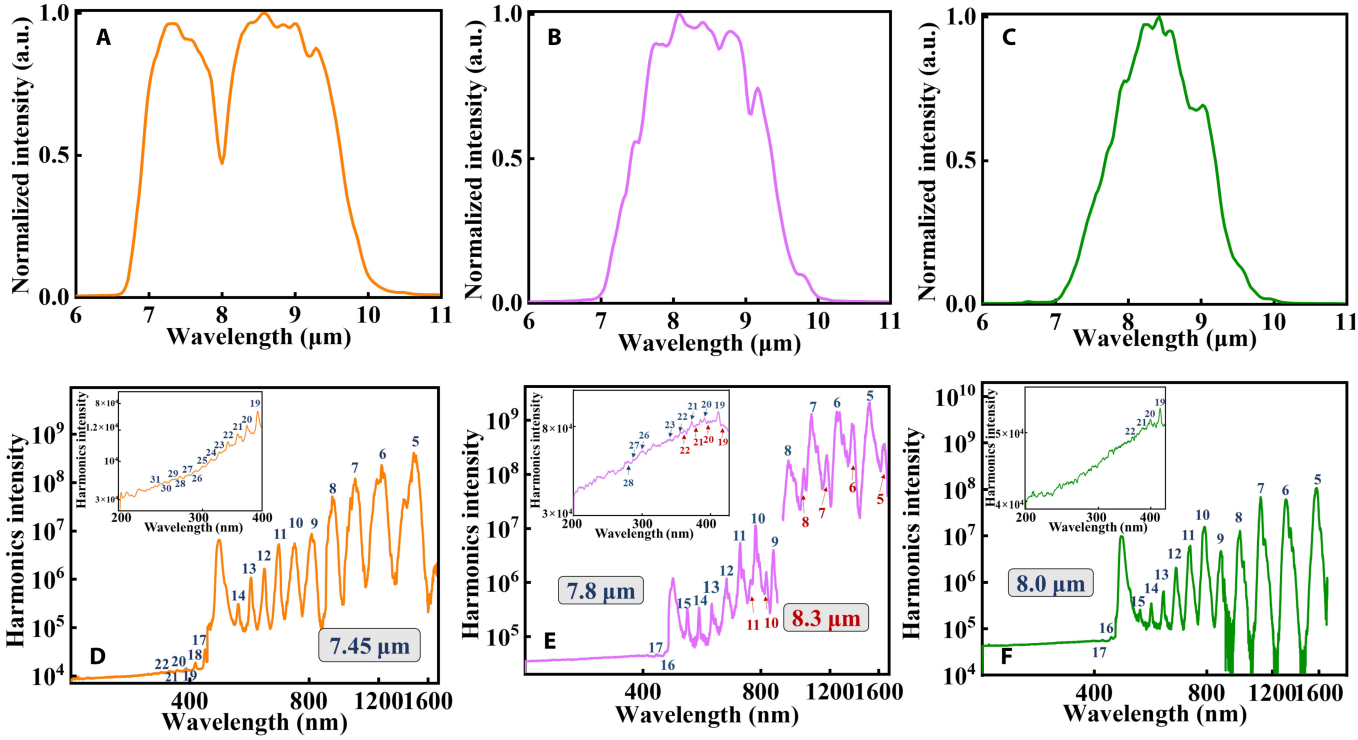

Fig. 8. The spectra of dual-wavelength MIR tunable pulses and its corresponding HHG spectra when the residual spectral chirp is fully compensated, and dual-wavelength bands of 7.3 and 9 μm are temporally overlapped. (A to C) The MIR spectra are shaped varying in the forms of dual-peak profile centered at (A) 7.3 and 9 μm, (B) flat-top shape, and (C) single peak centered at 8.2 μm, via tuning the pump delay. (D to F) The corresponding HHG spectra. As the MIR fundamental spectrum changes from a dual-wavelength to a flat-top, and to a single-peak shape, the corresponding HHG spectra exhibit single-set HHG in (D) with the fundamental wavelength of 7.45 μm, 2 sets of HHG in (E) with the fundamental wavelength of 7.8 and 8.3 μm, and another single set HHG in (F) with the fundamental wavelength of 8.0 μm. The insets in (D) to (F) respectively show the zoomed-in HHG spectra in the DUV regime.

HHG. As presented in Fig. 8A to C, the generated MIR spectra could be shaped to various profiles in the forms of the dual peaks centered at 7.3 and 9 μm, flat-top shape, and a single-peak spectrum centered at 8.2 μm, via tuning the pump delay while keeping the PM angle unchanged. The corresponding HHG spectra are shown in Fig. 8D to F. When the 2 spectral bands in the dual-peak spectrum have similar amplitude, as shown in Fig. 8D, a single HHG set of 7.45 μm is measured. We suggest that this is because the HHG efficiency drops abruptly as the driving wavelength increases, such that the measured HHG signal of 9 μm is suppressed when the driving wavelengths of 7.3- and 9-μm bands have similar intensity. By adjusting the pump delay, the MIR fundamental spectrum getting into a flat-top shape, as plotted in Fig. 8B, which is merged by dual-wavelength components of 7.8 and 8.3 μm. As measured in Fig. 8E, the HHG spectral peaks become broader, and eventually, double peaks are exhibited, corresponding to the fundamental wavelengths of 7.8 and 8.3 μm. The blue shift of the fundamental wavelengths in the harmonics sets pumped by the broadband dual-wavelength pulse is attributed to the higher HHG efficiency driven at shorter wavelengths. Further tuning the pump delay, the MIR spectrum centered at 8.0 μm and its corresponding HHG are exhibited as shown in Fig. 8F. In addition, the HHG spectra in the deep ultraviolet (DUV) region with harmonics up to the 31st order corresponding to a wavelength of 240 nm are measured, pumped by dual-wavelength MIR pulses, as shown in the insets of Fig. 8D to F. Further extension to shorter wavelengths is prohibited by our spectral measurement apparatus. However, it is worth mentioning that extreme ultraviolet HHG in solids has been demonstrated pumped by the MIR light with similar wavelength, pulse width, and intensity [34].

Conclusion

In conclusion, we have demonstrated a highly desirable dual-wavelength MIR femtosecond light source and spectral shaping technique with a relatively simple and compact apparatus compared to traditional pulse synthesizers. MIR spectral pairs tunable over a wavelength range of 5.6 to 11.4 μm are generated, and the full freedom in adjusting the relative amplitudes of the dual wavelengths is demonstrated. As a direct application, driven by dual-wavelength MIR femtosecond pulses, spectra of HHG in solids are shaped with substantial flexibility. The demonstrated spectral and temporal shaping technique generates passively stable carrier-envelope phase. Unlike existing dispersion control techniques used in parametric amplifiers such as the acousto-optic programmable dispersive filter, the demonstrated spectral and temporal shaping technique could be fed with pulses with high-power and large energy, which is a special merit beneficial for large-scale laser facilities. MIR ultrashort pulses with outstanding freedom in multiwavelength spectral shaping can trigger more advanced applications such as field-steered ionization and ultrafast electron tunneling in the field of strong-field physics. Moreover, experiments of lasers and nonlinear optics such as intrapulse difference-frequency generation, broadband terahertz-wave supercontinuum generation [35–37], controlling electron localization in molecular dissociation, and microprocessing of biomedical materials could be pursued with

bright prospects. Finally, steering HHG in solids driven by dual-wavelength MIR pulses could find special applications. For example, making use of the ultra-broadband spectrum in the DUV region with tunable spectral shapes, applications such as quasi-supercontinuum generation from MIR to DUV (even extreme ultraviolet) [38], optical coherence tomography in the DUV region [39], and DUV multispectral imaging [40] could be pursued. Moreover, in the time domain, the delay between MIR dual wavelengths could be precisely controlled; thus, by scanning the dual-wavelength MIR pulses or making use of the pump-and-probe HHG spectroscopy, the HHG pumped by dual-wavelength MIR OPA is useful for high-resolution diffraction-limited images for multispectral components [41] and HHG spectroscopic experiments for controlling phases of matter by coherently manipulating specific vibrational modes [42,43].

Acknowledgments

Funding: This work was supported by the National Natural Science Foundation of China (62075144 and U22A2090), Sichuan Outstanding Youth Science and Technology Talents (2022JDJQ0031), and Engineering Featured team Fund of Sichuan University (2020SCUNG105). **Author contributions:** H.L. conceived the idea. L.H., W.W., K.T., M.X., and Z.W. conducted the experiment. L.H. and F.Y. did the simulation. H.W. and H.L. analyzed the data. Z.-Y.C., L.H., and H.L. wrote the manuscript. L.H. and W.W. contributed equally. All authors discussed the results and contributed to the manuscript. **Competing interests:** The authors declare that they have no competing interests.

Data Availability

The corresponding author can provide relevant data if the demand is reasonable.

References

1. Krüger M, Schenk M, Hommelhoff P. Attosecond control of electrons emitted from a nanoscale metal tip. *Nature*. 2011;475:78–81.
2. Yoshioka K, Katayama I, Arashida Y, Ban A, Kawada Y, Konishi K, Takahashi H, Takeda J. Tailoring single-cycle near field in a tunnel junction with carrier envelope phase-controlled terahertz electric fields. *Nano Lett*. 2018;18(8):5198–5204.
3. Rybka T, Ludwig M, Schmalz MF, Knittel V, Brida D, Leitenstorfer A. Sub-cycle optical phase control of nanotunnelling in the single-electron regime. *Nat Photonics*. 2016;10:667–670.
4. Ludwig M, Aguirregabiria G, Ritzkowsky F, Rybka T, Marinica DC, Aizpurua J, Borisov AG, Leitenstorfer A, Brida D. Sub-femtosecond electron transport in a nanoscale gap. *Nat Phys*. 2020;16:341–345.
5. Krausz F, Stockman MI. Attosecond metrology: From electron capture to future signal processing. *Nat Photonics*. 2014;8(6):205–213.
6. Hassan MT, Luu TT, Moulet A, Raskazovskaya O, Zhokhov P, Garg M, Karpowicz N, Zheltikov AM, Pervak V, Krausz F, et al. Optical attosecond pulses and tracking the nonlinear response of bound electrons. *Nature*. 2016;530:66–70.
7. Chipperfield LE, Robinson JS, Tisch JWG, Marangos JP. Ideal waveform to generate the maximum possible electron Recollision energy for any given oscillation period. *Phys Rev Lett*. 2009;102(6):Article 063003.
8. Jin C, Wang G, Wei H, Le A-T, Lin CD. Waveforms for optimal sub-keV high-order harmonics with synthesized two- or three-colour laser fields. *Nat Commun*. 2014;5:Article 4003.
9. Li X, Fan J, Ma J, Wang G, Jin C. Application of optimized waveforms for enhancing high-harmonic yields in a three-color laser-field synthesizer. *Opt Express*. 2019;27(2):841–854.
10. Taniuchi T, Nakanishi H. Collinear phase-matched terahertz-wave generation in GaP crystal using a dual-wavelength optical parametric oscillator. *J Appl Phys*. 2004;95(12):Article 7588.
11. Kling MF, Siedschlag C, Verhoef AJ, Khan JI, Schultze M, Uphues T, Ni Y, Uiberacker M, Drescher M, Krausz F, et al. Control of electron localization in molecular dissociation. *Science*. 2006;312(5771):246–248.
12. Movasaghi Z, Rehman S, Rehman IU. Fourier transform infrared (FTIR) spectroscopy of biological tissues. *Appl Spectrosc Rev*. 2008;43(2):134–179.
13. Edwards G, Logan R, Copeland M, Reinisch L, Davidson J, Johnson B, Maciunas R, Mendenhall M, Ossoff R, Tribble J, et al. Tissue ablation by a free-electron laser tuned to the amide II band. *Nature*. 1994;371:416–419.
14. Perry MD, Crane JK. High-order harmonic emission from mixed fields. *Phys Rev A*. 1993;48(6):Article R4051.
15. Watanabe S, Kondo K, Nabekawa Y, Sagisaka A, Kobayashi Y. Two-color phase control in tunneling ionization and harmonic generation by a strong laser field and its third harmonic. *Phys Rev Lett*. 1994;73(20):2692–2695.
16. Huang S-W, Cirmi G, Moses J, Hong KH, Bhardwaj S, Birge JR, Chen LJ, Li E, Eggleton BJ, Cerullo G, et al. High-energy pulse synthesis with sub-cycle waveform control for strong-field physics. *Nat Phys*. 2011;5:475–479.
17. Krauss G, Lohss S, Hanke T, Sell A, Eggert S, Huber R, Leitenstorfer A. Synthesis of a single cycle of light with compact erbium-doped fibre technology. *Nat Photonics*. 2010;4:33–36.
18. Rossi GM, Mainz RE, Yang Y, Scheiba F, Silva-Toledo MA, Chia SH, Keathley PD, Fang S, Mücke OD, Manzoni C, et al. Sub-cycle millijoule-level parametric waveform synthesizer for attosecond science. *Nat Photonics*. 2020;14:629–635.
19. Wirth A, Hassan MT, Grguras I, Gagnon J, Moulet A, Luu TT, Pabst S, Santra R, Alahmed ZA, Azzeer AM, et al. Synthesized light transients. *Science*. 2011;334(6053):195–200.
20. Timmers H, Sabbar M, Hellwagner J, Kobayashi Y, Neumark DM, Leone SR. Polarization assisted amplitude gating as a route to tunable, high-contrast single attosecond pulses. *Optica*. 2016;3(7):707–710.
21. Yang Y, Mainz RE, Rossi GM, Scheiba F, Silva-Toledo MA, Keathley PD, Cirmi G, Kärtner FX. Strong-field coherent control of isolated attosecond pulse generation. *Nat Commun*. 2021;12:Article 6641.
22. Luu TT, Garg M, Kruchinin SY, Moulet A, Hassan MT, Goulielmakis E. Extreme ultraviolet high-harmonic spectroscopy of solids. *Nature*. 2015;521:498–502.
23. Garg M, Zhan M, Luu TT, Lakhotia H, Klostermann T, Guggenmos A, Goulielmakis E. Multi-petahertz electronic metrology. *Nature*. 2016;538:359–363.
24. Kaneshima K, Ishii N, Takeuchi K, Itatani J. Generation of carrier-envelope phase-stable mid-infrared pulses via dual-wavelength optical parametric amplification. *Opt Express*. 2016;24(8):8660–8665.

25. Liang H, Krogen P, Wang Z, Park H, Kroh T, Zawilski K, Schunemann P, Moses J, DiMauro LF, Kärtner FX, et al. High-energy mid-infrared sub-cycle pulse synthesis from a parametric amplifier. *Nat Commun*. 2017;8:141.
26. Ridente E, Weidman M, Mamaikin M, Jakubeit C, Krausz F, Karpowicz N. Hybrid phase-matching for optical parametric amplification of few-cycle infrared pulses. *Optica*. 2020;7(9):1093–1096.
27. Kim YW, Shao T-J, Kim H, Han S, Kim S, Ciappina M, Bian X-B, Kim S-W. Spectral interference in high harmonic generation from solids. *ACS Photonics*. 2019;6(4):851–857.
28. Goh SJ, Reinink J, Tao Y, van der Slot PJM, Bastiaens HJM, Herek JL, Biedron SG, Milton SV, Boller KJ. Spectral control of high-harmonic generation via drive laser pulse shaping in a wide-diameter capillary. *Opt Express*. 2016;24(2):1604–1615.
29. Qu S, Liang H, Liu K, Zou X, Li W, Wang QJ, Zhang Y. 9 μm few-cycle optical parametric chirped-pulse amplifier based on $LiGaS_2$. *Opt Lett*. 2019;44(10):2422–2425.
30. Xiao Y, Agrawal GP, Maywar DN. Nonlinear pulse propagation: A time-transformation approach. *Opt Lett*. 2012;37(7):1271–1273.
31. Martinez O. 3000 times grating compressor with positive group velocity dispersion: Application to fiber compensation in 1.3-1.6 μm region. *IEEE J Quantum Electron*. 1987;23(1):59–64.
32. Penwell SB, Whaley-Mayda L, Tokmakoff A. Single-stage MHz mid-IR OPA using $LiGaS_2$ and a fiber laser pump source. *Opt Lett*. 2018;43(6):1363–1366.
33. Qu S, Nagar GC, Li W, Liu K, Zou X, Luen SH, Dempsey D, Hong K-H, Wang QJ, Zhang Y, et al. Long-wavelength-infrared laser filamentation in solids in the near-single-cycle regime. *Opt Lett*. 2020;45(8):2175–2178.
34. Ghimire S, DiChiara AD, Sistrunk E, Agostini P, DiMauro LF, Reis DA. Observation of high-order harmonic generation in a bulk crystal. *Nat Phys*. 2011;7:138–141.
35. Koulouklidis AD, Gollner C, Shumakova V, Fedorov VY, Pugžlys A, Baltuška A, Tzortzakis S. Observation of extremely efficient terahertz generation from mid-infrared two-color laser filaments. *Nat Commun*. 2020;11:Article 292.
36. Mitrofanov AV, Sidorov-Biryukov DA, Nazarov MM, Voronin AA, Rozhko MV, Shutov AD, Ryabchuk SV, Serebryannikov EE, Fedotov AB, Zheltikov AM. Ultraviolet-to-millimeter-band supercontinua driven by ultrashort mid-infrared laser pulses. *Optica*. 2020;7(1):15–19.
37. Jang D, Schwartz RM, Woodbury D, Griff-McMahon J, Younis AH, Milchberg HM, Kim KY. Efficient terahertz and Brunel harmonic generation from air plasma via mid-infrared coherent control. *Optica*. 2019;6(10):1338–1341.
38. Wünsche M, Fuchs S, Aull S, Nathanael J, Möller M, Rödel C, Paulus GG. Quasi-supercontinuum source in the extreme ultraviolet using multiple frequency combs from high-harmonic generation. *Opt Express*. 2017;25(6):6936–6944.
39. Fuchs S, Wünsche M, Nathanael J, Abel JJ, Rödel C, Biedermann J, Reinhard J, Hübner U, Paulus GG. Optical coherence tomography with nanoscale axial resolution using a laser-driven high-harmonic source. *Optica*. 2017;4(8):903–906.
40. Shapiro DA, Yu Y-S, Tyliszczak T, Cabana J, Celestre R, Chao W, Kaznatcheev K, Kilcoyne ALD, Maia F, Marchesini S, et al. Chemical composition mapping with nanometre resolution by soft X-ray microscopy. *Nat Photonics*. 2014;8:765–769.
41. Witte S, Tenner VT, Noom DWE, KSE E. Lensless diffractive imaging with ultra-broadband table-top sources: From infrared to extreme-ultraviolet wavelengths. *Light Sci Appl*. 2014;3(3):Article e163.
42. Rini M, Tobey R, Dean N, Itatani J, Tomioka Y, Tokura Y, Schoenlein RW, Cavalleri A. Control of the electronic phase of a manganite by mode-selective vibrational excitation. *Nature*. 2007;449:72–74.
43. Disa AS, Nova TF, Cavalleri A. Engineering crystal structures with light. *Nat Phys*. 2021;17:1087–1092.